Journal of Materials Science & Technology 130 (2022) 112–123

Contents lists available at ScienceDirect

Journal of Materials Science & Technology

journal homepage: www.elsevier.com/locate/jmst

Research Article

Effect of static annealing on superplastic behavior of a friction stir welded Ti-6Al-4V alloy joint and microstructural evolution during deformation

C.L. Jia[a,b], L.H. Wu[a,b,c,*], P. Xue[a,c], D.R. Ni[a,b], B.L. Xiao[a,b], Z.Y. Ma[a,b,*]

[a] Shi-Changxu Innovation Center for Advanced Materials, Institute of Metal Research, Chinese Academy of Sciences, Shenyang 110016, China
[b] School of Materials Science and Engineering, University of Science and Technology of China, Shenyang 110016, China
[c] Key Laboratory of Nuclear Materials and Safety Assessment, Institute of Metal Research, Chinese Academy of Sciences, Shenyang 110016, China

ARTICLE INFO

Article history:
Received 18 February 2022
Revised 19 April 2022
Accepted 4 May 2022
Available online 30 May 2022

Keywords:
Friction stir welding
Titanium alloys
Superplasticity
Static annealing
Microstructure

ABSTRACT

Structural integration is one of the most critical developing directions in the modern aerospace field, in which large-scale complex components of Ti alloys are proposed to be fabricated via the method of welding + superplastic forming. However, the undesired strain localization appeared during superplastic deformation of the entire joint has largely hindered the development of this method. In our study, a combination process of friction stir welding (FSW) + static annealing + superplastic deformation was first time proposed to eliminate severe local deformation. To achieve this result, a fully fine lamellar structure was obtained in the nugget zone (NZ) via FSW, which was totally different from the mill-annealed structure in the base material (BM). After annealing at 900 °C for 180 min, the BM and NZ then exhibited the similar elongation of > 500% and similar flow stress at 900 °C, 3×10^{-3} s^{-1}, which was the precondition for achieving uniform superplastic deformation in the entire joint. Moreover, the different microstructures in the BM and NZ tended to become the similar equiaxed structure after deformation, which was the result of different microstructural evolution mechanisms in the NZ and BM. For the NZ, there was a static and dynamic spheroidization of the fully lamellar structure during the process, which could largely reduce the flow softening of the fully lamellar structure. For the BM, a new view of "Langdon-CRSS theory" (CRSS, critical resolved shear stress) was proposed to describe the fragmentation of the coarse equiaxed structure, which established the relationship between grain boundary sliding and intragranular deformation during deformation.

1. Introduction

Structural integration has become one of the most critical developing directions in the modern aerospace field. Superplastic forming (SPF) of titanium (Ti) alloys which is widely used in industrial manufacturing can fabricate complex components to reduce the weight and cost [1,2]. However, when there is the fabrication need for super large-scale integrated Ti alloy components, the manufacturing process is hardly fulfilled by SPF of a single sheet itself, since the width of the rolled Ti alloy sheets is limited. In order to solve this problem, the combination of SPF and welding technique, i.e. SPF applied on the welded large-scale sheet, has attracted great attentions [3–6].

Recently, various fusion welding methods such as laser welding [7], tungsten inert gas welding (TIG) [8], have been attempted on the SPF of Ti alloys. Generally speaking, to ensure a uniform SPF on the whole weld, the similar superplastic abilities, especially the similar flow stress in each zone of the welded joint is highly required. In general, the mill-annealed Ti alloy base material (BM) with a fine equiaxed microstructure exhibits a good superplasticity, whereas only a coarse lamellar structure is obtained in the fusion welded zone, which exhibits much higher flow stress and lower elongation for the welded zone than the BM [9,10]. As a result, during SPF of the entire joint, a severe local deformation would occur in the BM while seldom deformation took place in the fusion welded zone.

Friction stir welding (FSW) as a solid state welding method [11], can produce the fine microstructure in the nugget zone (NZ) be-

* Corresponding authors at: Shi-Changxu Innovation Center for Advanced Materials, Institute of Metal Research, Chinese Academy of Sciences, Shenyang 110016, China.
E-mail addresses: lhwu@imr.ac.cn (L.H. Wu), zyma@imr.ac.cn (Z.Y. Ma).

https://doi.org/10.1016/j.jmst.2022.05.006
1005-0302/

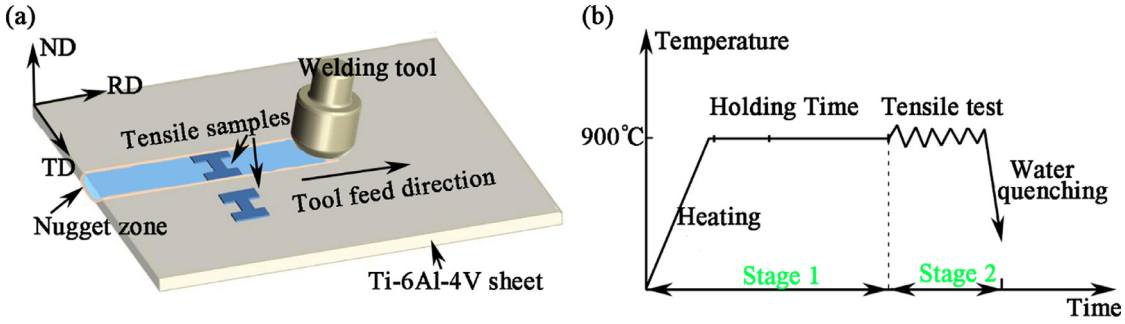

Fig. 1. (a) Schematic of friction stir welding process and sample positions, (b) heating process during superplastic tensile test.

cause the materials experienced severe plastic deformation and dynamic recrystallization [12,13]. For example, a fine fully lamellar structure would be generally obtained in the NZ of FSWed joints in most parameters, which was reported to exhibit an excellent superplasticity of $>$ 700% [14,15]. Therefore, FSW is a promising method to maintain the excellent superplasticity in the NZ as that in the BM. However, it is still difficult to achieve a similar superplastic ability including the elongation and flow stress in the two zones, since the NZ shows the totally different microstructure from the BM [16,17].

Recently, studies [18] showed that the similar superplasticity could be obtained by different microstructures. It showed that a comparable elongation ($>$ 395%) could be obtained for the BM with the mill-annealed structure and for the NZ with the fine lamellar structure at 800 °C and 3 $\times$ 10^{-4} s^{-1}. However, the discrepancy of the initial flow stress between the BM and NZ still existed and the NZ always showed a higher flow stress than the BM at the initial deformation stage.

It was reported that the flow stress of the joint could be decreased by the thermohydrogen process [19–21]. However, the thermohydrogen process is costly, and the hydrogenation and dehydrogenation processes are complicated and time-consuming. Moreover, the flow stress of the BM and NZ might be decreased simultaneously after the thermohydrogen process. Thus, the similar superplastic flow stress is still not easy to be obtained in the BM and NZ even after the thermohydrogen process. Therefore, uniform deformation of the entire joint still could not be obtained. So how to obtain the similar superplastic deformation ability, especially the similar flow stress by different microstructures is still the main problem.

Generally, the similar superplastic abilities could be obtained by the similar microstructures for the BM and NZ. However, it is difficult to obtain the similar microstructure in the BM and NZ directly because of the severe deformation in the NZ by FSW. The spheroidization process of the lamellar structure in the NZ is a possible method to obtain the equiaxed structure which is similar to the equiaxed structure in the BM [16]. There exists two classical spheroidization theories for the lamellar structure in Ti alloys. One is the static spheroidization theory, which is known as the termination migration model [22]. The other is the dynamic spheroidization theory, which exhibits as the boundary splitting model [23]. The α/β interface with the Burgers orientation relationship (BOR) for the lamellar structure is very stable and is difficult to be broken without the assistance of pre-deformation for the spheroidization [24]. However, the process of pre-deformation is difficult to be controlled and would change the properties of the BM greatly. Therefore, the similar microstructure is also difficult to be obtained for the BM and NZ without greatly changing of the microstructure in the BM.

It was reported that the fine lamellar structure could be spheroidized during the static annealing process without pre-deformation, and the fraction of spheroidization for lamellae obtained by FSW increased from 2.2% to 20.8% after annealing at 800 °C [14]. Our previous study [25] also pointed out that lamellae could be spheroidized only by static annealing through the migration of the adjacent lamellae. So for the lamellar structure in the NZ, there was a possibility to obtain an equiaxed structure by static annealing without changing the equiaxed structure in the BM greatly.

Although it is still difficult to achieve the similar structure of the BM and NZ by static annealing, there is a trend for the similar superplastic abilities for the mill-annealed structure in the BM and the lamellar structure in the NZ after static annealing for a certain time [25]. Therefore, it is necessary to further evaluate the microstructure evolution and superplastic abilities for the BM and NZ by static annealing for the entire joint.

In the study, the Ti-6Al-4V sheet was welded via FSW to obtain the fully lamellar structure in the NZ, and static annealing was carried on the entire joint. The superplastic abilities for the BM and NZ were then evaluated after static annealing for different time. It aims to (a) investigate the effect of the static annealing process on the superplastic abilities for the BM and NZ, and (b) evaluate the deformation mechanisms for the equiaxed structure in the BM and the lamellar structure in the NZ during the superplastic deformation process.

2. Experimental

The 2 mm thick mill-annealed Ti-6Al-4V alloy sheet was used as the BM. A W-25Re welding tool with a shoulder of 11 mm in diameter and a tapered pin of 1.65 mm in length was used. In order to obtain the fully lamellar structure, the sheet was friction stir welded at a rotation rate of 500 rpm and a traverse speed of 150 mm/min. The Ni-base superalloy was utilized as the backplate. The argon gas was employed to protect the sheet from being oxidized during FSW.

In the study, the reference directions were simplified as follows: ND, the normal direction; TD, the traverse direction; RD, the rolling direction. During the FSW process, the feed direction was parallel to the rolling direction. The AS and RS represented as the advancing side and retreating side, respectively. The tensile samples were cut from the NZ and the BM. The FSW process and the positions of tensile samples were shown in Fig. 1(a). The tensile specimens were heated at a speed of 10 °C/min until it reached 900 °C. The specimens were then held in the furniture for 5, 60 and 180 min before superplastic deformation as shown in Fig. 1(b). The annealing time was selected just referring to our previous study [25]. The BM annealing for 5 min and 180 min before tension was simplified as BM-5 and BM-180, respectively. The NZ annealing for 5 min and 180 min before deformation was simplified as NZ-5 and NZ-180, respectively.

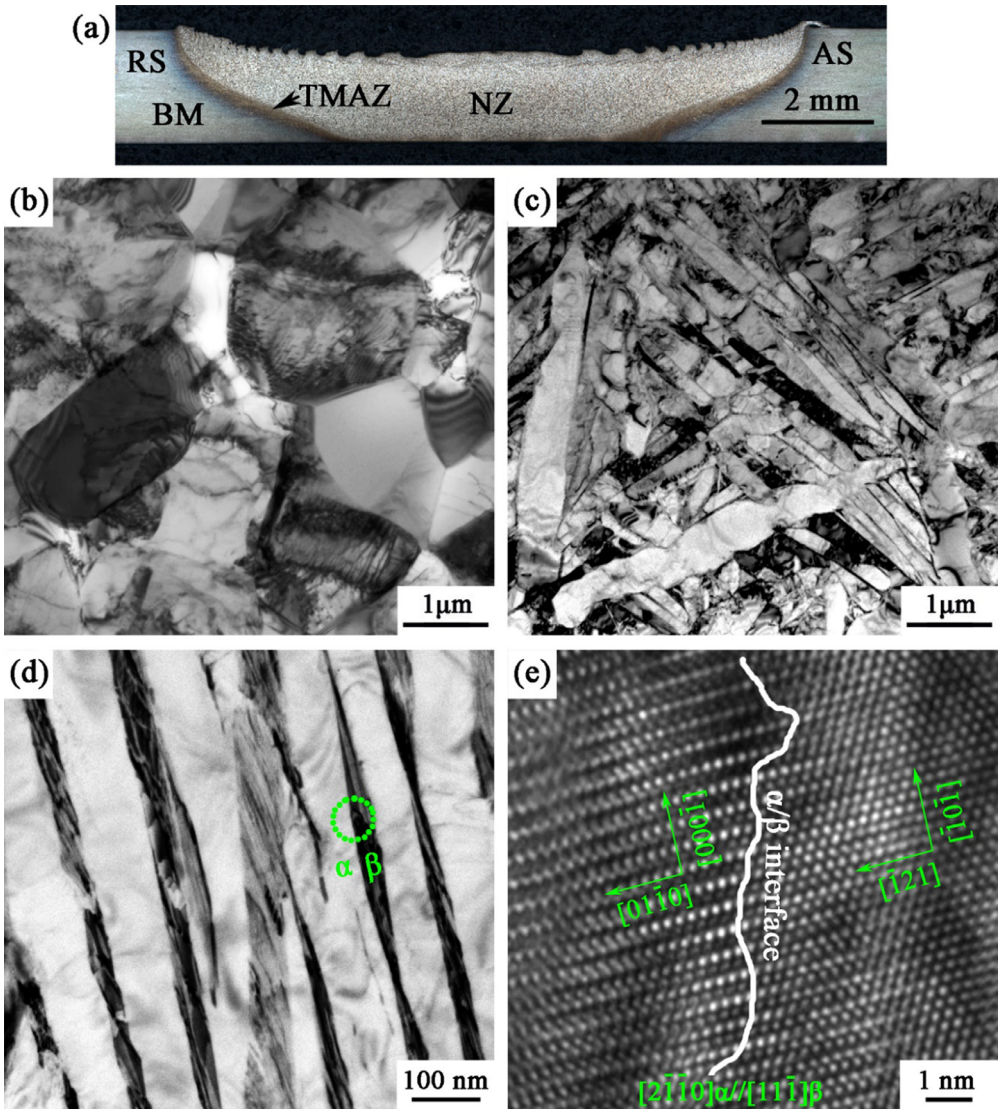

Fig. 2. (a) Cross-section of friction stir welded Ti-6Al-4V joint, and transmission electron microscope (TEM) images of: (b) base material (BM) and (c, d) nugget zone (NZ), and (e) high resolution transmission electron microscope (HR-TEM) image for marked lamellar structure in (d).

Referring to our previous studies [14,25], 900 °C was selected as the temperature for annealing and superplatic deformation in this study. The tensile test was applied at 900 °C and at the strain rates of 1×10^{-4} s^{-1}, 3×10^{-4} s^{-1}, 1×10^{-3} s^{-1} and 3×10^{-3} s^{-1}. Moreover, the specimens were interrupted when the engineering strain reached 0, 40, 200% at a strain rate of 3×10^{-3} s^{-1}. The specimens were quenched into the water immediately after static annealing or high-temperature tension. The high-temperature holding process before deformation was defined as the stage 1 and the superplastic deformation process was defined as the stage 2 as shown in Fig. 1(b).

The microstructure was characterized using scanning electron microscopy (SEM), transmission electron microscopy (TEM) and electron backscatter diffraction (EBSD). The specimens for SEM were ground, polished and then etched with a solution of Kroll's reagent. TEM and EBSD samples were prepared by double-jet electrolytic polishing with a chemical solution of 6 mL $HClO_4$ + 34 mL CH_3OH + 60 mL C_4H_9OH at −25 °C. In order to statistically analyze the grain size and the fraction of spheroidized grains, the thickness and length of more than 300 of the α lamellae and equiaxed α grains were measured, respectively.

3. Results

3.1. Microstructure of the as-received material and nugget zone

After FSW, a defect-free joint was obtained, as shown by the cross-section of the friction stir welded joint in Fig. 1(a). The welded joint contained three typical zones: the BM, the NZ and the thermo-mechanically affect zone (TMAZ). The TMAZ was very narrow as shown in Fig. 2(a) because of the low thermal conductivity for the Ti alloys [26]. Fig. 2(b) exhibits the mill-annealed structure for the BM. The BM mainly consisted of the equiaxed α structure and the β phase. The average α grain size in the BM was about 2.2 μm. Some sub-boundaries were also found inside α grains. After FSW, a fully lamellar structure was obtained in the NZ (Fig. 2(c)). The fully lamellar structure implied that the welding parameter exceeded the β transus temperature. The average thickness of the lamellar α were 180 ± 70 nm. The high resolution TEM (HR-TEM) in Fig. 2(e) showed that the direction of $[2\bar{1}\bar{1}0]_\alpha$ for the α phase was parallel to that of $[11\bar{1}]_\beta$ for the β phase. There existed the BOR for the lamellar α and β phase in the NZ of the FSW joint in this study, which exhibits as: $\{0001\}_\alpha$ //$\{110\}_\beta$, $<11\bar{2}0>_\alpha$//

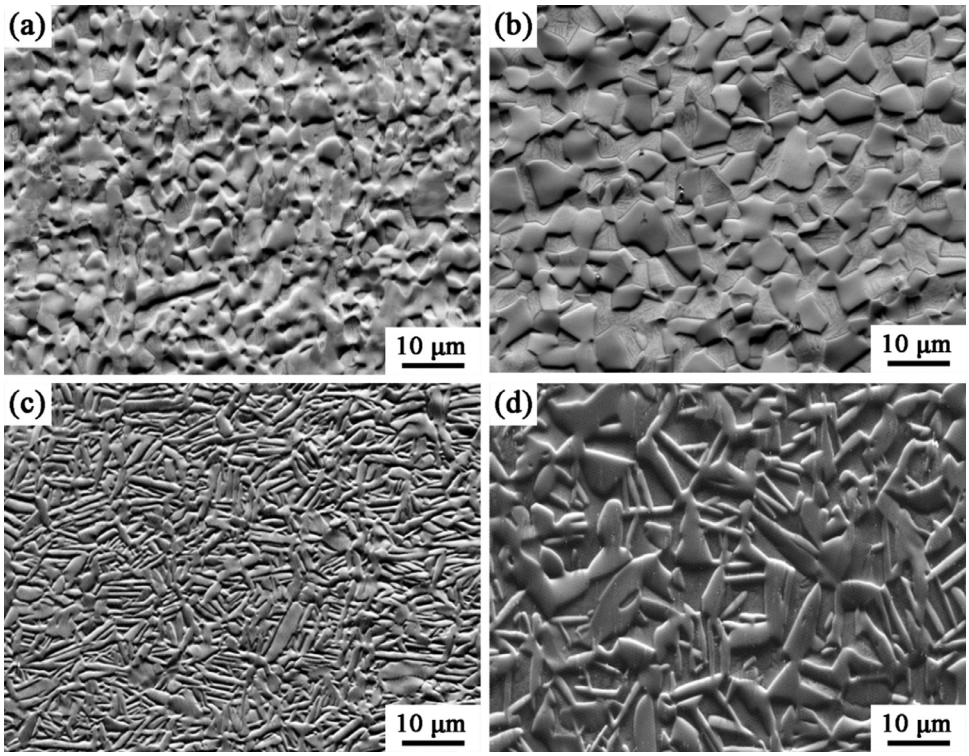

Fig. 3. Scanning electron microscope (SEM) images of (a, b) BM and (c, d) NZ after annealing at 900 °C for (a, c) 5 min, (b, d) 180 min, respectively.

$<111>_{\beta}$. The details have been reported by our previous studies [25].

3.2. Microstructure evolution during the static annealing process prior to deformation

Fig. 3(a) and (b) show the microstructure of the BM after annealing for 5 and 180 min before deformation. After annealing for 5 min, the slight grain growth occurred for the α structure and the average grain growth exhibited to be about 3.07 μm. While after annealing for 180 min as shown in Fig. 3(b), obvious coarsening occurred for the α grains, and the average grain size was about 5.98 μm. Furthermore, during static annealing, the α grains exhibited the feature of the coarsening of the coarse grains and the shrink of the fine grains, which was known as the Ostwald ripening (OR) theory during annealing [30]. The grain size varied from 1.34 to 7.44 μm.

Fig. 3(c) and (d) exhibit the microstructure of the NZ after annealing for 5 and 180 min before superplastic deformation. After annealing for 5 min, the structure remained the lamellar morphology. Some equiaxed α grains appeared in the lamellar structure. The spheroidized α grains (the spheroidized grain was defined when the aspect ratio was less than 2) accounted for less than 30.0%. After annealing for 180 min, the fraction of the spheroidized grains increased to be about half of the total lamellar structure, and become the mixed structure containing both the lamellar structure and equiaxed structure.

3.3. High-temperature properties after static annealing

Fig. 4(a) exhibits the true stress-strain curves of the BM and NZ annealing at 900 °C for different time at the strain rate of 3×10^{-3} s^{-1}. For the BM and NZ after annealing for 5 min, the initial flow stress of the NZ was higher than that of the BM. However, at the later deformation stage, the flow stress of the NZ became lower than that of the BM. When the true strain reached 0.75, there was an intersection for the stress-strain curves of the BM and NZ. With the increase of the holding time, the initial peak flow stress approached and became similar after holding for 180 min. The true tress-strain curves of the BM and NZ were also similar after annealing for 180 min and both exhibited as the slight flow softening characters after the peak flow stress. With the extension of the strain rates and the holding time, the initial flow stress approached gradually and became similar at the strain rate of 3×10^{-3} s^{-1} and after holding for 180 min.

Fig. 4(b) shows the variation of the initial flow stress at the true strain of 0.1 with the strain rate after different annealing time. The m value in Fig. 4(b) represented the strain rate sensitivity exponent. When the annealing time increased from 5 to 180 min, the m values of the BM decreased from 0.66 to 0.60, and it reduced from 0.44 to 0.39 for the NZ with the annealing time increasing at the strain rates from 3×10^{-4} s^{-1} to 3×10^{-3} s^{-1}. It was reported that when the m value exceeded 0.3, the superplastic deformation was dominated by the grain boundary sliding (GBS) [27]. Therefore, the main deformation mechanisms for both of the lamellar structure and the equiaxed one might be both related to the GBS.

Fig. 5(a) shows the initial flow stress at 900 °C, 3×10^{-3} s^{-1} and the average grain size (the grain size of the lamellar structure was represented by the thickness of lamellae) for the BM and NZ after different annealing time. With the increase of the holding time, the initial flow stress for the BM exhibited a higher growth rate than the NZ. Therefore, although the NZ showed higher initial flow stress than the BM when annealing for 5 min, the lower growth rate of the initial flow stress for the NZ than the BM during prolong static annealing contributed to the possibility of nearly the same initial flow stress during high-temperature tension. The lower increase rate of the initial flow stress for the NZ than the BM was related to the lower coarsening rates for the lamellar structure in the NZ than the equiaxed structure in the BM (Fig. 5(a)).

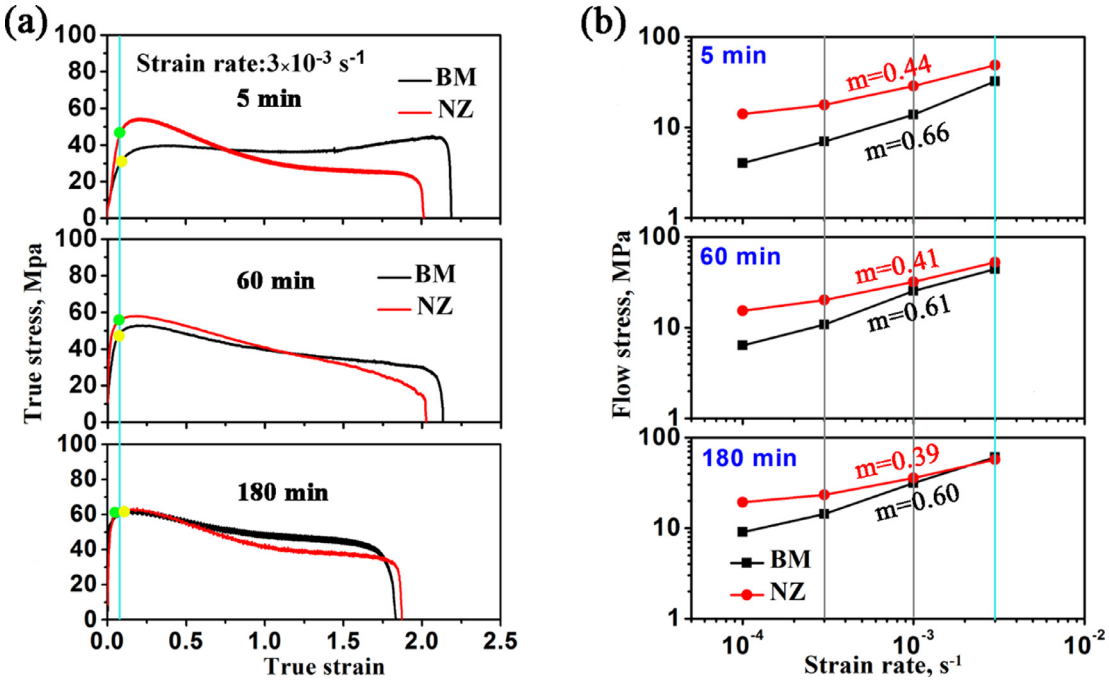

Fig. 4. Superplastic flow stress of BM and NZ after annealing at 900 °C for 5, 60 and 180 min: (a) true stress-strain curves of BM and NZ at 900 °C, 3 × 10^{-3} s^{-1}, (b) variation of flow stress at true strain of 0.1 with strain rate from 1 × 10^{-4} s^{-1} to 1 × 10^{-2} s^{-1}. The flow stress for the BM and NZ at 1 × 10^{-3} s^{-1} in (b) has been reported in Ref. [25].

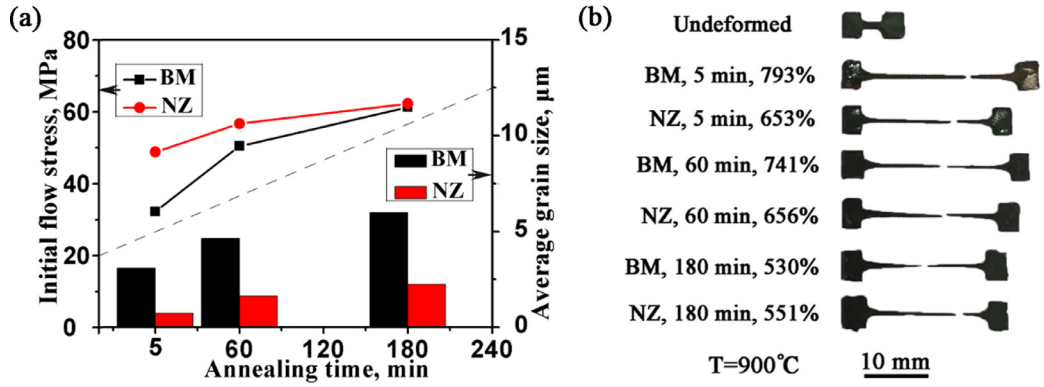

Fig. 5. (a) Variation of initial flow stress and average grain size with annealing time, and (b) macroscopic tensile specimens after fracture at 900 °C, 3 × 10^{-3} s^{-1} for BM and NZ after annealing for different times.

The α/β interface for the lamellar structure followed the BOR and exhibited as the low-energy interface as shown in Fig. 2(e). However, there didn't exist the BOR for the equiaxed structure in the BM. Therefore, the grain growth for the lamellar structure was constrained during static annealing, exhibiting a lower grain growth rate than the equiaxed structure in the BM [28,29].

The macroscopic morphologies of the fracture samples at 900 °C, 3 × 10^{-3} s^{-1} are shown in Fig. 5(b). At all the parameters, the features of the uniformly deformation were presented. When the annealing time increased from 5 to 180 min, the elongations for both the BM and NZ decreased, which was attributed to the grain coarsening with the annealing time increasing. For comparison, the decrease degree for the elongation of the BM was more evident than that of the NZ. The reason was that the equiaxed structure in the BM showed a higher coarsening rate than the lamellae in the NZ (Fig. 5(a)), which led to a greater reduction for the elongations in the BM. The elongations for the BM and NZ were presented to be similar after annealing for 180 min at 3 × 10^{-3} s^{-1} and the elongations for both of them exceeded 500%.

3.4. Microstructure evolution at different engineering strains

The true strains of 0.33 (engineering strain of 40%) and 1.09 (engineering strain of 200%) were selected as the typical true strains at the stage of less than and greater than 0.75 (the transition point in Fig. 4(a)), respectively. The microstructures of the BM-5, NZ-5 at the engineering strain of 0, 40 and 200% are shown in Fig. 6. For the BM-5 before deformation in Fig. 6(a), the microstructure exhibited to be equiaxed with a rolling orientation character. When the engineering strain increased to be 200%, the microstructure remained equiaxed and the orientation of the microstructure became random. For the NZ-5 in Fig. 6(d), the microstructure performed as the lamellar structures with a feature of random orientation. However, nearly all the lamellar structures were spheroidized to be the equiaxed ones at the engineering strain of 200% as shown in Fig. 6(f), which was known as the dynamic spheroidization process during deformation [23].

Moreover, with the increase of the strain, the fraction of low angle grain boundaries (LAGBs) increased first and then decreased for BM-5 and NZ-5, as shown in Fig. 6. With the increase of the

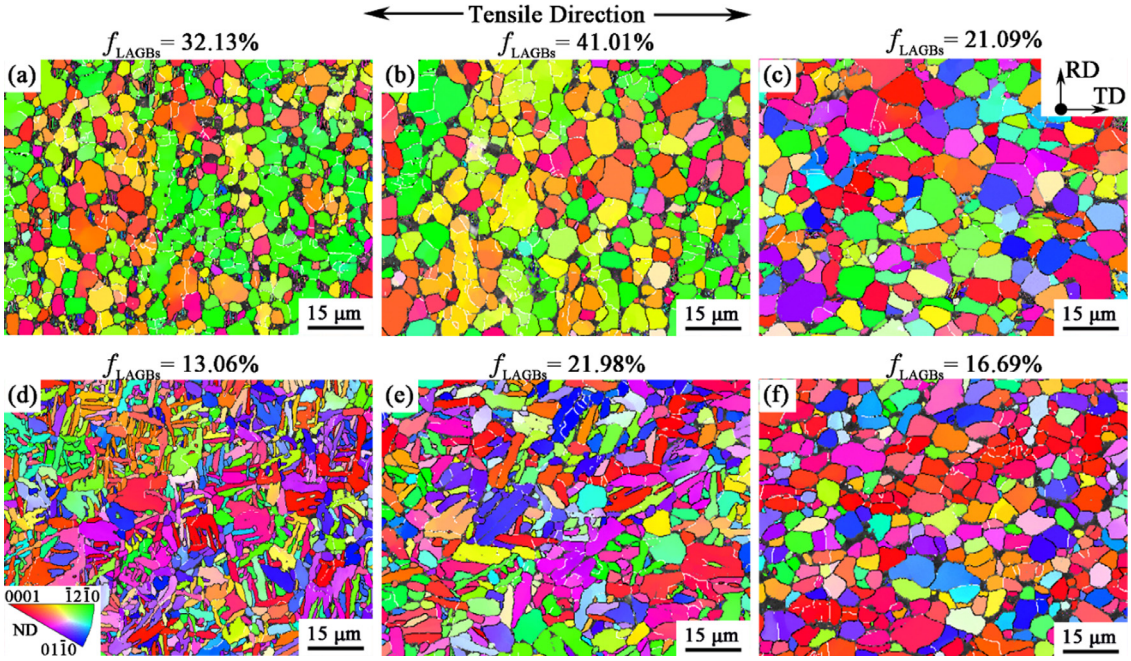

Fig. 6. Inverse pole figure (IPF) maps of (a–c) BM and (d–f) NZ at engineering strain of (a, d) 0%, (b, e) 40% and (c, f) 200% after annealing for 5 min before deformation, respectively.

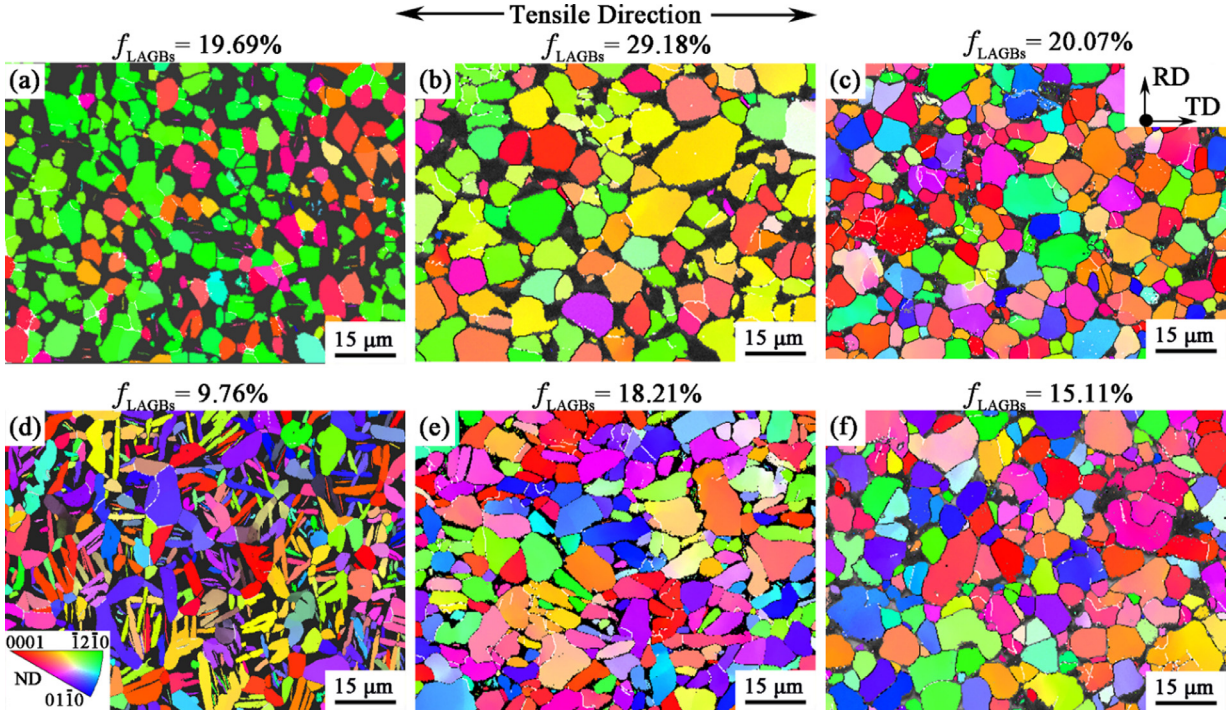

Fig. 7. IPF maps of (a–c) BM and (d-f) NZ at engineering strain of (a, d) 0%, (b, e) 40% and (c, f) 200% after annealing for 180 min before deformation, respectively.

holding time as shown in Fig. 7(a) and (b), the fraction of the LAGBs decreased more significantly for the BM-180 and NZ-180 before deformation, compared with that of the microstructure in the BM-5 and NZ-5 (Fig. 6(a) and (d)). When the engineering strain increased to be 200%, the mixed structure changed to be the fully equiaxed structure and the microstructure feature in the NZ-180 was similar to that of the BM-180 at the engineering strain of 200%. Moreover, the fraction of the LAGBs also showed a trend of increasing first and then decreasing with the increase of the strain.

Fig. 8 exhibits the statistical data for the microstructure of the BM and NZ during stage 1 and stage 2 (Stage 1 represented the static annealing process and stage 2 exhibited the dynamic deformation process, which was shown in Fig. 1(b)). During the early deformation stage with the engineering strain of 40%, the grains for the BM-5, NZ-5, BM-180 and NZ-180 performed to be a clear coarsening behavior, compared to those without deformation. However, when the engineering strain further increased from 40 to 200%, the coarsening rate decreased and a character of

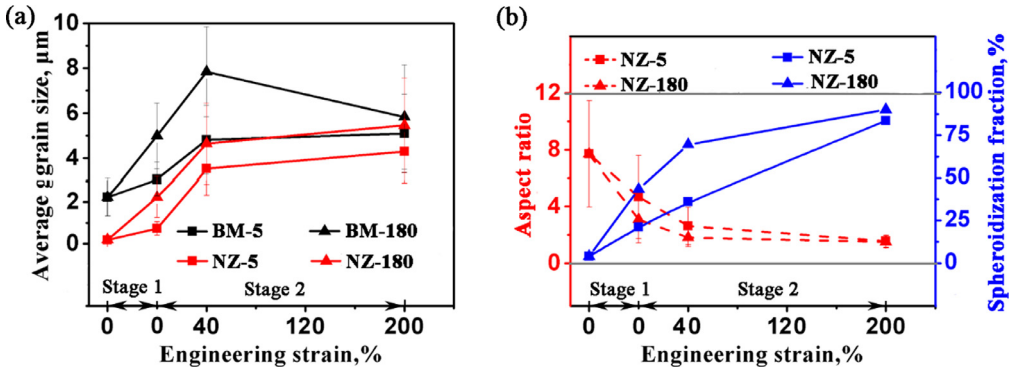

Fig. 8. Variation of (a) average grain size for BM and NZ, and (b) aspect ratio and spheroidization fraction for lamellar structure in NZ with engineering strain.

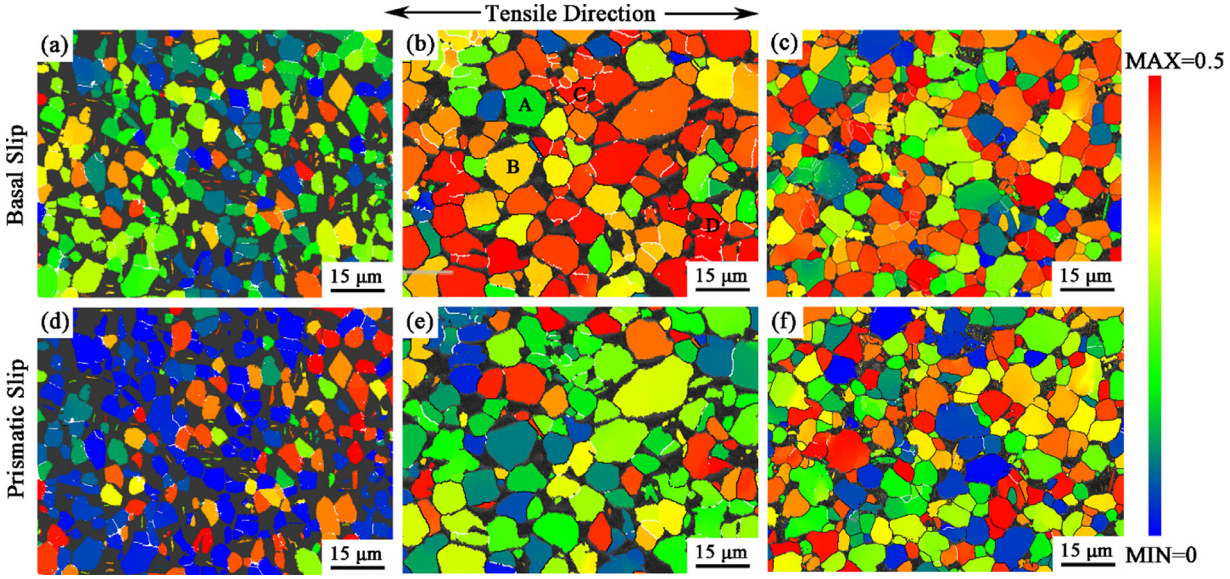

Fig. 9. Schmid factor evolution for basal slip and prismatic slip of BM at engineering strain of (a, d) 0%, (b, e) 40% and (c, f) 200% after annealing for 180 min before deformation, respectively.

grain refinement even exhibited at the BM-180 during deformation (Fig. 8(a)).

Compared with the average grain size for the BM-180 in Fig. 7(c) and the NZ-180 in Fig. 7(f) before deformation, there existed a trend for the similar grain size and grain morphology for the BM-180 and NZ-180 at the engineering strain of 200%. The results implied that different microstructures such as the BM and NZ for the entire joint not only could perform as the similar superplastic behavior but also could exhibit a trend to be a similar microstructure during superplastic deformation. Thus, the process could further eliminate the inhomogeneous structure in the welded joint and obtain a homogeneous structure after deformation. So the process has potential to greatly improve the performance of the large-scale Ti alloy components.

3.5. Schmid factor evolution for the BM and NZ during deformation

Figs. 9 and 10 show the Schmid factors for the basal <a> and prismatic <a> slip systems along the tensile direction of the α grains in the BM-180 and NZ-180 at engineering strains of 0, 40% and 200%. Under the applied stress, the activity for the slip system was closely related to the Schmid factor and the critical resolved shear stress (CRSS) [30]. The higher Schmid factor implied the lower CRSS for the same slip system.

For the BM-180, when the engineering strain increased from 0 to 40% as shown in Fig. 9(a) and (b), there were an evident change for the Schmid factors of grains with the basal <a> slip along the tensile direction, and most grains tended to exhibit a high Schmid factor for the basal slip. Moreover, nearly all the LAGBs (the white lines inside grains) were shown in the grains with the maximum Schmid factor, which implied that the basal slip was activated in the α grains with the less CRSS in the same slip system. For example, the grain A and grain B exhibited as the coarser grains in Fig. 9(b), bur the LAGBs didn't appear inside the grains because of the lower Schmid factor. Instead, LAGBs exhibited in the finer grains such as grain C and grain D with higher Schmid factor along the tensile direction for the basal slip.

The evolution of the Schmid factor for the α grains with the prismatic slip was less clear than that of the basic slip along the tensile direction as shown in Fig. 9(d) and (e). LAGBs appeared in the grains with both the high and low Schmid factor for the prismatic slip at the engineering strain of 40%. For the NZ-180, it contained both the lamellar structure and equiaxed structure. There was also a feature that most grains with a high Schmid factor exhibited the basal slip along the tensile direction at the engineering strain of 40% (Fig. 10(b)). LAGBs trended to appear in the grains with the maximum Schmid factor for both the basal slip and the prismatic slip as shown in Fig. 10(b) and (e).

The average Schmid factors for the basal slip and prismatic slip of the BM-5, NZ-5, BM-180 and NZ-180 were calculated and shown in Fig. 11. For the basal slip in Fig. 11(a), the average Schmid factor changed little for the lamellar structure in the NZ-5 at the ini-

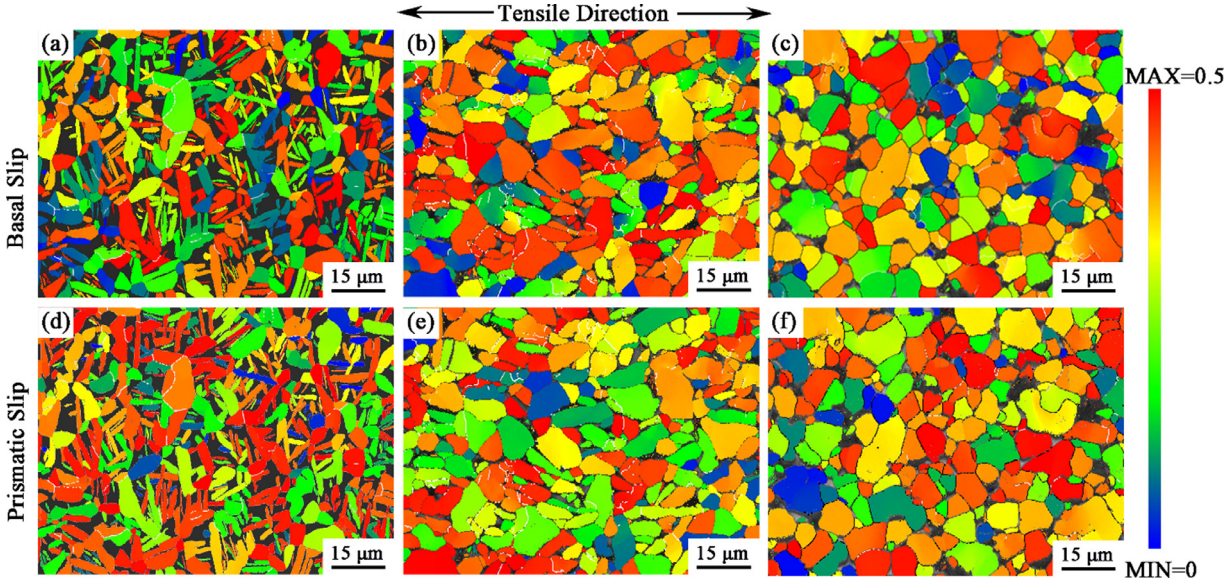

Fig. 10. Schmid factor evolution for basal slip and prismatic slip of NZ at engineering strain of (a, d) 0%, (b, e) 40% and (c, f) 200% after annealing for 180 min before deformation, respectively.

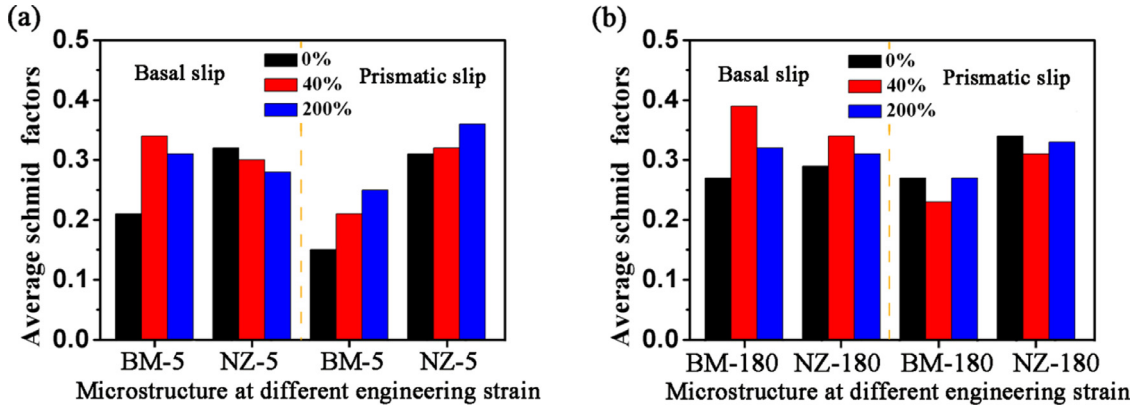

Fig. 11. Average Schmid factor evolution along tensile direction for (a) basal and (b) prismatic slip of BM and NZ during superplastic deformation.

tial deformation stage. For the NZ-180, introducing equiaxed structure into the lamellar structure contributed to the more evident variation of the average Schmid factor for the basal slip along the tensile direction (Fig. 11(a)). With the further improvement for the proportion of the equiaxed structure in the BM-5 and BM-180, the variation of the average Schmid factor became more evident at the initial deformation stage for the basal slip, which implied that the proportion of GBS was improved with the increase of the ratio for the equiaxed structure. For the prismatic slip in Fig. 11(b), at the initial deformation stage, the variation of the average Schmid factor for the NZ-5 and the BM-5 of the prismatic slip was similar to that of the basal slip. For the BM-180 and NZ-180 the average Schmid factor decreased for the prismatic slip along the tensile direction at the initial deformation stage.

For the equiaxed structure, the deformation was closely related to the GBS, and the rotation for the equiaxed structure resulted in the evident change for the average Schmid factor. However, GBS was difficult to be activated for the lamellar structure because of the non-equiaxed morphology [31,32]. Therefore, during the deformation process, different slip systems were activated in similar proportions because of the random orientation for the lamellar structure in the NZ. When some equiaxed structures were introduced in the fully lamellar structure to become the mixed structure as shown in Fig. 11(b) for the NZ-180, the deformation model changed. The average Schmid factor exhibited more evident change for the mixed structure in the NZ-180 than that of the lamellar structure in the NZ-5, which implied that GBS could be reactivated for the NZ-180 by introducing some equiaxed grains in to the fully lamellar structure. Most importantly, the microstructure with a large amount of equiaxed structure all showed the same deformation feature: equiaxed α structure tended to rotate towards the high Schmid factor in the basal slip system along the tensile direction. The result was consistent with the distribution of the Schmid factor for the microstructure in Figs. 9(b) and 10(b).

Fig. 12 shows the <0002> pole figure of the Schmid factor along the tensile direction and texture evolution for the BM-5 and BM-180 at the engineering strain of 0%, 40% and 200%, respectively. For the BM, the pole figure of the BM-5 and BM-180 before deformation exhibited a typical mill-annealed feature with the c-axis of α grains parallel to the TD (Fig. 12(a) and (d)). When the engineering strain increased to be 40% as shown in Fig. 12(b) and (e), the pole with the maximum intensity shifted and the position of the pole was consistent with the grains with the maximum Schmid factor for the basic <a> slip. These features were marked by the black arrows. When the engineering strain increased from 40 to 200%, a homogeneous orientation distribution was observed

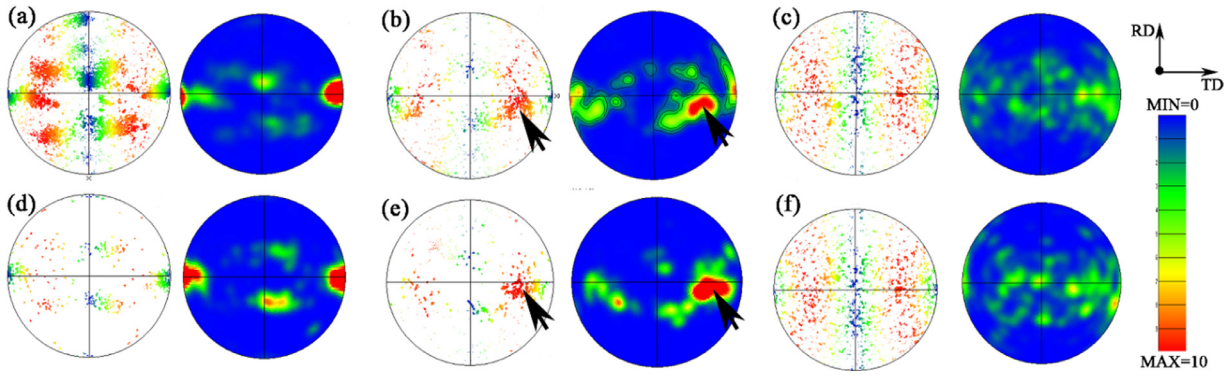

Fig. 12. <0002> pole figure for a distribution of Schmid factor of the basal slip in left and texture in right for (a–c) BM-5 and (d–f) BM-180 and at an engineering strain of (a, d) 0%, (b, e) 40% and (c, f) 200% during superplastic deformation.

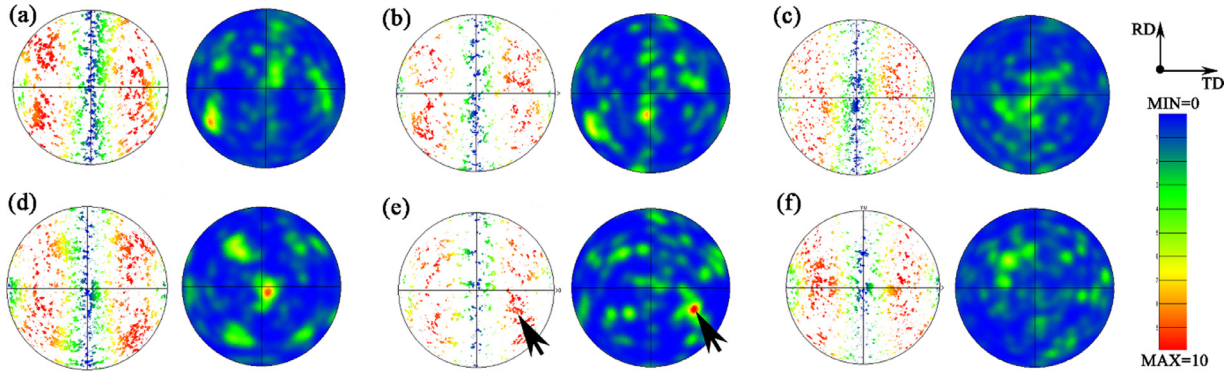

Fig. 13. <0002> pole figure for a distribution of Schmid factor for the basal slip in left and texture in right for (a–c) NZ-5 and (d–f) NZ-180 and at an engineering strain of (a, d) 0%, (b, e) 40% and (c, f) 200% during superplastic deformation.

(Fig. 12(c) and (f)) both for the BM-5 and BM-180 and the texture was greatly weakened. The weakening of texture should be result of GBS and rotation of grains during deformation [33].

Fig. 13 exhibits the <0002> pole figure of the Schmid factor along the tensile direction and texture evolution for the NZ-5 and NZ-180 at the engineering strain of 0%, 40% and 200%, respectively. For the NZ-5 and NZ-180, the texture were weak before deformation, which implied that the orientation of the lamellar structure and the mixed structure was more random than that of the mill-annealed BM. When the engineering strain increased to be 40%, there was no significant change for the texture of the lamellar structure in the NZ-5. However, a pole generated in the pole figure for the mixed structure of the NZ-180 at the engineering strain of 40%. The position of the pole for the NZ-180 was consistent with the position of grains with the maximum Schmid factor for the basic <*a*> slip, which was similar to the character of the texture evolution for the BM-5 and BM-180, although the intensity of the texture for the NZ-180 was weaker than that of the BM-5 and BM-180.

It was reported that the texture weakness was a typical character for the GBS during the superplastic deformation process [33,34]. The result in our study showed that the texture weakening was only the result of the later deformation stage. At the early deformation stage, the equiaxed structure trended to rotate to be the high Schmid factor in the basal slip system along the tensile direction and further to form to be the special texture as shown in Figs. 12(b), (e) and 13(e). The coarser the average grain size, the higher the intensity of the texture (Fig. 8(a)). Moreover, LAGBs formed in the grains with high Schmid factor for the basal slip (Figs. 9(b) and 10(b)), which were related to the dislocation accommodation inside the grains [35].

4. Discussion

4.1. GBS-induced dislocation accommodation for the equiaxed structure during deformation

Generally speaking, the flow behaviors of the materials during superplastic deformation are separated into three regions, which is considered as region I, II, and III. The region II is generally defined by high *m* value and the deformation mechanism is closely related to GBS [35].

Rachinger GBS [36] is related to a rigid grain movement, and the grain movement is accommodated by the dislocation activities. Langdon [37,38] further extended the dislocation accommodation theory and proposed that the process was controlled by the subgrain size parameter λ. When the grain size is less than that of the calculated λ, the deformation is accommodated by GBS; when the grain size is larger than that of the calculated λ, intragranular deformation occurs and subgrain boundaries forms inside the large grains. The Langdon theory was reported to be in excellent agreement with the experimental observation [35,39].

To better understand the result in our study, the Langdon theory was applied in the research. The equation for the Langdon theory could be explained as [27]:

$$\frac{\lambda}{b} = \zeta \left(\frac{\sigma}{\mu}\right)^{-1} \tag{1}$$

In the equation, b presents as the magnitude of Burgers' vector, μ exhibits as the shear modulus, σ is the applied stress, and ζ is a constant value. The subgrain size λ is determined by σ.

According to the Eq. (1), the calculated subgrain size λ exhibited to be 4.07 and 5.20 MPa for the BM-180 when the engineering

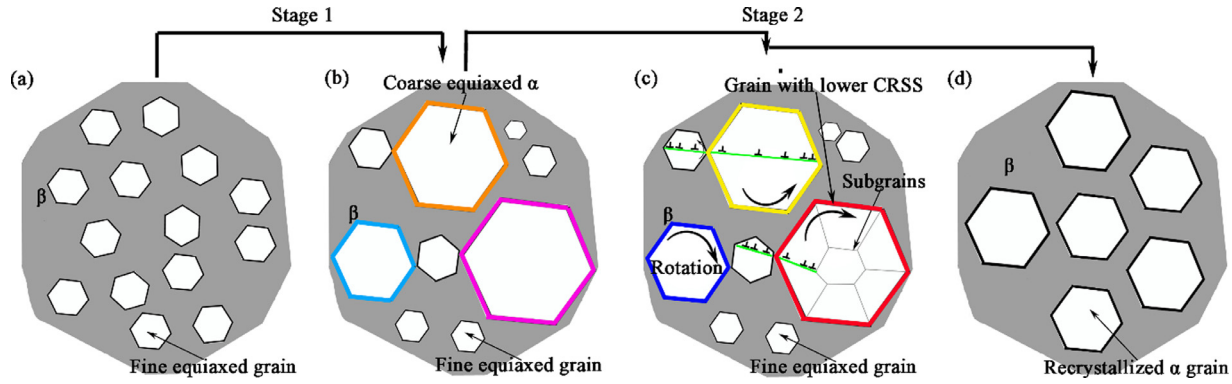

Fig. 14. Schematic of microstructural evolution in BM during annealing and subsequent deformation: (a) initial microstructure for BM, (b) grain coarsening for BM after static annealing, (c) intragranular deformation occurred in coarse grains with lower CRSS, (d) coarse grains occurred recrystallization to be smaller ones.

strain reached 40% and 200%. The actual experimental grain size in our study performed to be 7.84 and 5.83 μm at the same engineering strain. When the engineering strain reached 40%, the experimental average grain size (7.84 μm) for the BM-180 was clear larger than that of the calculated subgrain size λ (4.07 μm), intragranular deformation occurred in some larger grain size. The fraction of LAGBs increased from 19.69 to 29.18%.

When the engineering strain reached 200%, the experimental average grain size (5.83 μm) for the BM-180 was similar to the calculated subgrain size λ (5.20 μm). Therefore, less intragranular deformation was supposed to occur, and the fraction of LAGBs decreased from 29.18 to 20.07%. Therefore, the result in our study is correspond to the Langdon theory to some degree. However, there are some points in the study different from the Langdon theory. As shown in Fig. 9(b) for the BM-180 at the engineering strain of 40%, LAGBs were only generated inside the grains with the maximum Schmid factor for the basal slip along the tensile direction, regardless of the grain size.

During the deformation process, there was a close link for the formation of the LAGBs and the CRSS in the slip system inside the grains. It was reported that the CRSS was lower for the basal slip and the prismatic slip during the deformation at 900 °C compared with other slip systems in the α phase of Ti alloys [40]. The results in the study exhibited that the intragranular deformation in equiaxed α grains formed to be the LAGBs and the deformation process was dominated by the basic $<a>$ slip at the early deformation stage.

Therefore, the model of the microstructure evolutions for the BM-180 at the static annealing process (stage 1) and the dynamic deformation stage (stage 2) are shown in Fig. 14. At the static annealing stage, there was a static coarsening feature for the α grains as shown in Figs. 3(b) and 14(c). During the dynamic deformation stage, LAGBs were generated inside some coarse grains, and then coarse grains were fragmented into the fine grains. However, not all the coarse grains would be fragmented immediately. LAGBs were generally generated inside the coarse grains with the maximum Schmid factor first (grains with the maximum Schmid factor were corresponded to the lowest CRSS along the tensile direction) for the basic slip system (Figs. 9(b) and 14(c)).

With the further rotation of grains, the Schmid factor for the coarse grains without intragranular deformation gradually changed from a relative low value to be the maximum. LAGBs then started to generate inside these grains. Therefore, coarse grains exhibited as a dynamic fragmentation process during the rotation of grains. Finally, nearly all the coarse grains were fragmented to be the fine grains, and the microstructure exhibited as the relatively uniform distribution of the grain size (Fig. 14(d)).

4.2. Spheroidization process of lamellar structure in the NZ

There was a static and dynamic spheroidization process of the lamellar structure at the static annealing stage (stage 1) and the dynamic deformation stage (stage 2) in the NZ. Finally, nearly all the lamellar structure changed to be the equiaxed structure in the later deformation stage (Fig. 7(f)). Fig. 15 shows the microstructure evolution model of the initial lamellar structure during the stage 1 and stage 2 process.

During the stage 1, the fraction of the spheroidization for lamellar structure increased and the average aspect ratio gradually decreased as the increase of the annealing time (Fig. 8(b)), which promoted that the change of the lamellar structure to be the equiaxed grains (Fig. 15(a)). The driving force for the static spheroidization of the lamellar structure came from the curvature difference between the termination and the flat interface for the lamellae [23]. However, there existed the BOR in the α and β phase for the lamellar structure [41]. The energy for the α/β interface with BOR performed to be very low and the interface was difficult to be broken during the static annealing process without prestrain. The low-energy interface could restrain the coarsening rate for the lamellar structure [24]. Therefore, the lamellar structure in the NZ exhibited a lower coarsening rate than the equiaxed structure in the BM (Fig. 5(a)).

During the stage 2, there was a dynamic spheroidization character for the mixed structure as shown in Figs. 3(d), 7(f) and 15. For the lamellar structure of the NZ-5, it showed a relatively random orientation before deformation (Fig. 7(d)). However, GBS was difficult to be activated for the lamellae because of the non-equiaxed morphology and the BOR in the α/β interface [42]. So at the initial deformation stage, the lamellar structure could not rotate to the specific orientation and the activation of the slip systems was also random, which led to the unclear change of the average Schmid factor for both the basal slip system and the prismatic slip system (Fig. 11(a)). By introducing the equiaxed structure into the lamellar structure, the deformation mechanism changed compared to that of the fully lamellar structure. The deformation character for the mixed structure was similar to that of the fully equiaxed structure for the BM-5 and BM-180 (Figs. 10 and 11), and the grains trended to rotate to the orientation with the higher Schmid factor for the basal slip along the tensile direction.

There was also a deformation accommodation for the lamellar structure and the equiaxed structure in the deformation process of the mixed structure (Fig. 15(c)). At the early deformation stage, although equiaxed structure exhibited as the GBS mechanism, lamellae were difficult to rotate, which induced the dislocation accumulation inside the lamellar structure and further to form the LAGBs

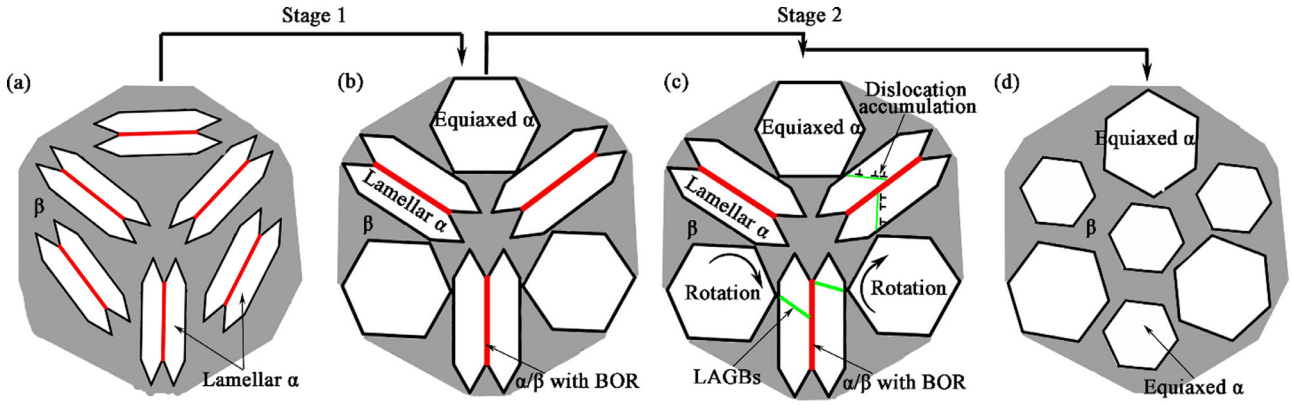

Fig. 15. Schematic of spheroidization process of lamellar structure in NZ during annealing and subsequent deformation: (a) fully lamellar structure in NZ, (b) static spheroidization for lamellar structure after static annealing, (c) dynamic spheroidization process for lamellar structure, (d) spheroidized grains after deformation.

(Figs. 7(e) and 15(c)). Finally, lamellar structure was fragmented into the equiaxed grain in the later deformation stage (Figs. 7(f) and 15(d)).

In summary, the new process of FSW + static annealing + superplastic tension was proposed in order to solve the problem of local tear for the entire joint during the superplastic deformation process. Firstly, the fully lamellar structure was obtained in the NZ by FSW. After static annealing for 180 min at 900 °C, similar superplastic abilities (including both the flow stress and the elongation) were obtained for the BM and NZ. Therefore, there was a possibility for the uniform deformation for the entire joint. Then, during the deformation process, there was a trend for the similar equiaxed microstructure for the BM and NZ, which implied that the inhomogeneous welded structure could change to be homogeneous equiaxed structure during the superplastic deformation process. Therefore, the new process proposed in the study provides a method which has the potential to fabricate large-scale weldless Ti alloy components. Furthermore, the deformation accommodation for the lamellar structure, the equiaxed structure and the structure consisting both lamellae and equiaxed grains were discussed, respectively.

5. Conclusions

By controlling the parameters of FSW, a fine fully lamellar structure was obtained in the NZ of the Ti-6Al-4V alloy joint. After annealing for different time before deformation, the superplastic behaviors and the deformation mechanisms of the mill-annealed structure for the BM and the lamellar structure in the NZ were studied. The conclusions were made as follows.

(1) After annealing at 900 °C for 180 min, the NZ and BM with different microstructures achieved the similar superplastic abilities including the similar flow stress and the close elongations of over 500% at 900 °C, 3×10^{-3} s^{-1}.
(2) During the deformation process, there was a trend for the inhomogeneous welded structure changing to be the homogeneous equiaxed structure by the fragmentation of the coarse equiaxed structure in the BM and the dynamic spheroidization process of the lamellar structure in the NZ.
(3) At the early deformation process of the equiaxed grains, GBS and the deformation accommodation induced the grains to rotate to the direction with the higher Schmid factor of the basal slip along the tensile direction as well as the generation of LAGBs inside the grains with the higher Schmid factor.
(4) The GBS-induced intragranular deformation was not only controlled by the grain size but also influenced by the CRSS, which provided an optimized view on the classical Langdon theory.

Acknowledgments

This work was supported by the National Natural Science Foundation of China (Nos. 51601194, 51471171) and the Youth Innovation Promotion Association of the Chinese Academy of Sciences (2021193 and Y2021061).

References

[1] Z.Q. Li, H.P. Guo, Mater. Sci. Forum 475-479 (2005) 3037–3042.
[2] A.J. Barnes, J. Mater. Eng. Perform. 16 (4) (2007) 440–454.
[3] M. Ramulu, P.D. Edwards, D.G. Sanders, A.P. Reynolds, T. Trapp, Mater. Des. 31 (6) (2010) 3056–3061.
[4] P.D. Edwards, D.G. Sanders, M. Ramulu, J. Mater. Eng. Perform. 19 (4) (2010) 510–514.
[5] P.D. Edwards, M. Ramulu, Sci. Technol. Weld. Join. 14 (5) (2013) 476–483.
[6] L. Ma, M. Wan, W. Li, J. Shao, X. Bai, J. Zhang, Mater. Sci. Eng. A 817 (2021) 141419.
[7] B. Kong, G. Liu, D. Wang, K. Wang, S. Yuan, Mater. Des. 90 (2016) 723–732.
[8] C. Homer, J.P. Lechten, B. Baudelet, Metall. Trans. A 8 (7) (1977) 1191–1193.
[9] S. Chen, J. Huang, D. Cheng, H. Zhang, X. Zhao, Mater. Sci. Eng. A 541 (2012) 110–119.
[10] B. Guo, S.L. Semiatin, J.J. Jonas, Mater. Sci. Eng. A 761 (2019) 138047.
[11] R.S. Mishra, Z.Y. Ma, Mater. Sci. Eng. R 50 (1-2) (2005) 1–78.
[12] L.H. Wu, X.B. Hu, X.X. Zhang, Y.Z. Li, Z.Y. Ma, X.L. Ma, B.L. Xiao, Acta Mater. 166 (2019) 371–385.
[13] Z.Y. Ma, A.L. Pilchak, M.C. Juhas, J.C. Williams, Scr. Mater. 58 (5) (2008) 361–366.
[14] L.H. Wu, B.L. Xiao, D.R. Ni, Z.Y. Ma, X.H. Li, M.J. Fu, Y.S. Zeng, Scr. Mater. 98 (2015) 44–47.
[15] W. Zhang, H. Liu, H. Ding, H. Fujii, Mater. Sci. Eng. A 785 (2020) 139390.
[16] W. Zhang, H. Liu, H. Ding, H. Fujii, J. Alloy. Compd. 803 (2019) 901–911.
[17] H. Mirzadeh, Mater. Sci. Eng. A 819 (2021) 141499.
[18] L.H. Wu, P. Xue, B.L. Xiao, Z.Y. Ma, Scr. Mater. 122 (2016) 26–30.
[19] H.J. Liu, L. Zhou, P. Liu, Q.W. Liu, Int. J. Hydrog. Energy 34 (11) (2009) 9596–9602.
[20] H.J. Liu, L Zhou, Q.W. Liu, Scr. Mater. 61 (11) (2009) 1008–1011.
[21] L.H. Wu, C.L. Jia, S.C. Han, N. Li, D.R. Ni, B.L. Xiao, Z.Y. Ma, M.J. Fu, Y.Q. Wang, Y.S. Zeng, J. Alloy. Compd. 787 (2019) 1320–1326.
[22] J. Xu, W. Zeng, H. Ma, D. Zhou, J. Alloy. Compd. 736 (2018) 99–107.
[23] S. Zherebtsov, M. Murzinova, G. Salishchev, S.L. Semiatin, Acta Mater. 59 (10) (2011) 4138–4150.
[24] M. Cabibbo, S. Zherebtsov, S. Mironov, G. Salishchev, J. Mater. Sci. 48 (3) (2012) 1100–1110.
[25] C.L. Jia, L.H. Wu, P. Xue, H. Zhang, D.R. Ni, B.L. Xiao, Z.Y. Ma, J. Mater. Sci. Technol. 119 (2022) 1–10.
[26] L.H. Wu, D. Wang, B.L. Xiao, Z.Y. Ma, Scr. Mater. 78-79 (2014) 17–20.
[27] H. Masuda, E. Sato, Acta Mater. 197 (2020) 235–252.
[28] S. Balachandran, A. Kashiwar, A. Choudhury, D. Banerjee, R. Shi, Y. Wang, Acta Mater. 106 (2016) 374–387.
[29] S.L. Semiatin, B.C. Kirby, G.A. Salishchev, Metall. Mater. Trans. A 35A (9) (2004) 2809–2819.
[30] S. Roy, S. Suwas, J. Alloy. Compd. 548 (2013) 110–125.
[31] J.H. Kim, S.L. Semiatin, C.S. Lee, Acta Mater. 51 (18) (2003) 5613–5626.
[32] T.K. Ha, Y.W. Chang, Acta Mater. 46 (8) (1998) 2741–2749.
[33] E. Alabort, D. Putman, R.C. Reed, Acta Mater. 95 (2015) 428–442.

[34] J. Han, S.H. Kang, S.J. Lee, M. Kawasaki, H.J. Lee, D. Ponge, D. Raabe, Y.K. Lee, Nat. Commun. 8 (1) (2017) 751.
[35] E. Alabort, P. Kontis, D. Barba, K. Dragnevski, R.C. Reed, Acta Mater. 105 (2016) 449–463.
[36] W.A. Rachinger, J. Inst. Met. 81 (1) (1952) 33–41.
[37] T.G. Langdon, Mater. Trans. 46 (9) (2005) 1951–1956.
[38] T.G. Langdon, Mater. Sci. Eng. A 283 (1–2) (2000) 266–273.
[39] T.G. Langdon, J. Mater. Sci. 41 (3) (2006) 597–609.
[40] G. Lütjering, J.C. Williams, Titanium, 2nd ed, Springer, NewYork, 2007.
[41] X. Zheng, S. Zheng, J. Wang, Y. Ma, H. Wang, Y. Zhou, X. Shao, B. Zhang, J. Lei, R. Yang, X. Ma, Acta Mater. 181 (2019) 479–490.
[42] S. Balachandran, S. Kumar, D. Banerjee, Acta Mater. 131 (2017) 423–434.